Structural Engineering Three-Dimensional Nano-Heterojunction Networks for High-Performance Photochemical Sensing

Zain Ul Abideen,[†] Jun-Gyu Choi,[†] Jodie A. Yuwono, Won-June Lee, Krishnan Murugappan, Priyank Vijaya Kumar, David R. Nisbet, Thành Trần-Phú, Myung-Han Yoon,* and Antonio Tricoli*

Read Online

ACCESS | Metrics & More | Article Recommendations | Supporting Information

ABSTRACT: Nanoscale heterojunction networks are increasingly regarded as promising functional materials for a variety of optoelectronic and photocatalytic devices. Despite their superior charge-carrier separation efficiency, a major challenge remains in the optimization of their surface properties, with surface defects playing a major role in charge trapping and recombination. Here, we report the effective engineering of the photocatalytic properties of nanoscale heterojunction networks via deep ultraviolet photoactivation throughout their cross-section. For the first time, in-depth XPS analysis of very thick ($\sim$10 μm) Ni_xO_y-ZnO films reveals localized p-n nanoheterojunctions with tunable oxygen vacancies (V_o) originating from both Ni_xO_y and ZnO nanocrystals. Optimizing the amount of oxygen vacancies leads to a 30-fold increase in the photochemoresistive response of these networks, enabling the detection of representative analyte concentrations down to 2 and 20 ppb at an optimal temperature of 150 °C and room temperature, respectively. Density functional theory calculations reveal that this performance enhancement is presumably due to an 80% increase in the analyte adsorption energy. This flexible nanofabrication approach in conjunction with straightforward vacancy control via photoactivation provides an effective strategy for engineering the photocatalytic activity of porous metal oxide semiconductor networks with applications in chemical sensors, photodetectors, and photoelectrochemical cells.

KEYWORDS: nanoscale heterojunctions, oxygen vacancy, room temperature sensing, deep ultraviolet photoactivation, ZnO-NiO, XPS, DFT
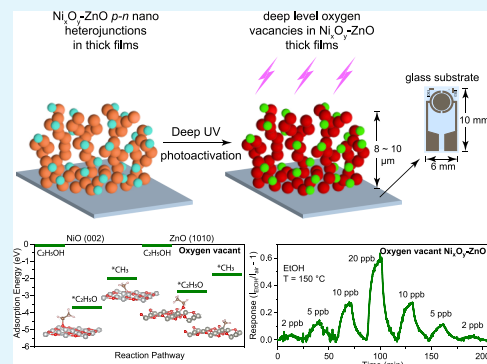
INTRODUCTION

Nanoscale heterojunctions have recently emerged as a promising multifunctional material platform. Among other benefits, the engineering of strong electrical field gradients in these nanoscale structures allows to attain nonconventional optical, electrical, and (electro)chemical properties that are not achievable with single semiconductor materials and their bulk heterojunctions.[1] Advances in the physics and fabrication of nanoscale heterojunctions are leading a renaissance in the architecture and composition of optoelectronic devices, demonstrating high-efficiency solar cells,[2] light-emitting diodes,[3] transistors,[4] biomolecular,[5] and chemical sensors[6] as well as potential for quantum computing and spintronics.[7] While significant progress has been made in the understanding of their electronic structure and energy level alignment,[8] the large specific surface of nanoscale heterojunctions is prone to induce trapping states and high recombination rates that may negatively impact device performance. Therefore, the judicious engineering of the surface composition of nanoscale heterojunctions is highly desired to realize their full potential in photochemical and optoelectronic applications.

The use of nanoscale heterojunctions for sensing has been pioneered by the engineering of one-[9] and zero-dimensional[10]

ZnO-NiO nanocomposite structures for visible-blind UV photodetectors, demonstrating vastly superior device performance such as enhanced detectivity, rise and recovery times. These findings have been translated into a variety of photocatalytic and optoelectronic applications, including the development of high-surface-area ZnO-NiO particle networks for low-temperature photochemical sensing.[11] The formation of NiO-Fe$_2$O$_3$ p-n nanoscale heterojunctions has also been reported to increase the chemoresistive response of α-Fe$_2$O$_3$ to toluene gas molecules by 7.8 times.[12] This was attributed to more efficient charge separation[10] and enhanced surface reaction kinetics. Similarly, electron−hole separation was reported at p-CuO/n-TiO$_2$ heterointerfaces, resulting in larger depletion zones and more dissociation of analytes.[13] Recently, Li et al.[14] reported an enhanced photocatalytic activity of ZnO-NiO heterojunctions for dye degradation, further indicating a
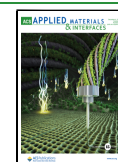
Table 1. Comparison of Recently Developed Chemical Sensors Based on Heterostructures with Oxygen Defects

Material	Sensing temperature (°C)	Oxygen vacancy introduction method	EtOH concentration (ppm)	Responsivity ($I_{EtOH}/I_{air} - 1$)	Detection limit (ppm)	ref
Porous Ni_xO_y-ZnO nanoscale heterojunction networks	RT[a]	Photoactivation at 200 °C	0.05	1.91	0.01	This work
			1	8.38		
	150	Photoactivation at 200 °C	1	22.45	0.002	This work
ZnO-NiO nano heterojunction	RT[a]	Without oxygen vacancies	1	2.6	0.01	11
Co-doped ZnO microspheres	220	Co-doping at 400 °C	5	3.3[b]	N/A	25
CeO_2-doped ZnO nanostructures	350	UV irradiation method, calcination at 600 °C	500	150[b]	N/A	26
Ce-doped ZnO nanostructures	300	Ce-doping at 450 °C	100	72.6[b]	N/A	27
ZnO/SnO_2 composite hollow spheres	225	Hydrothermal process, calcination at 400 °C	30	34.8[b]	0.5	28
ZnO-In_2O_3 nanostructures	250	Solution synthesis, calcination at 400 °C	300	900[b]	N/A	29
ZnO added MoO_3 nanostructures	300	Sputtering, annealing at 500 °C	300	38[b]	N/A	30
Tb-SnO_2 nanotubes	200	Electrospinning process, calcination at 500 °C	100	53.6[b]	1	31
CdO-loaded ZnO nanostructures	250	Hydrothermal process, annealing at 500 °C	100	65.5[b]	0.5	32
CeO_2 decorated SnO_2 hollow spheres	225	Hydrothermal process, calcination at 400 °C	100	37[b]	10	33

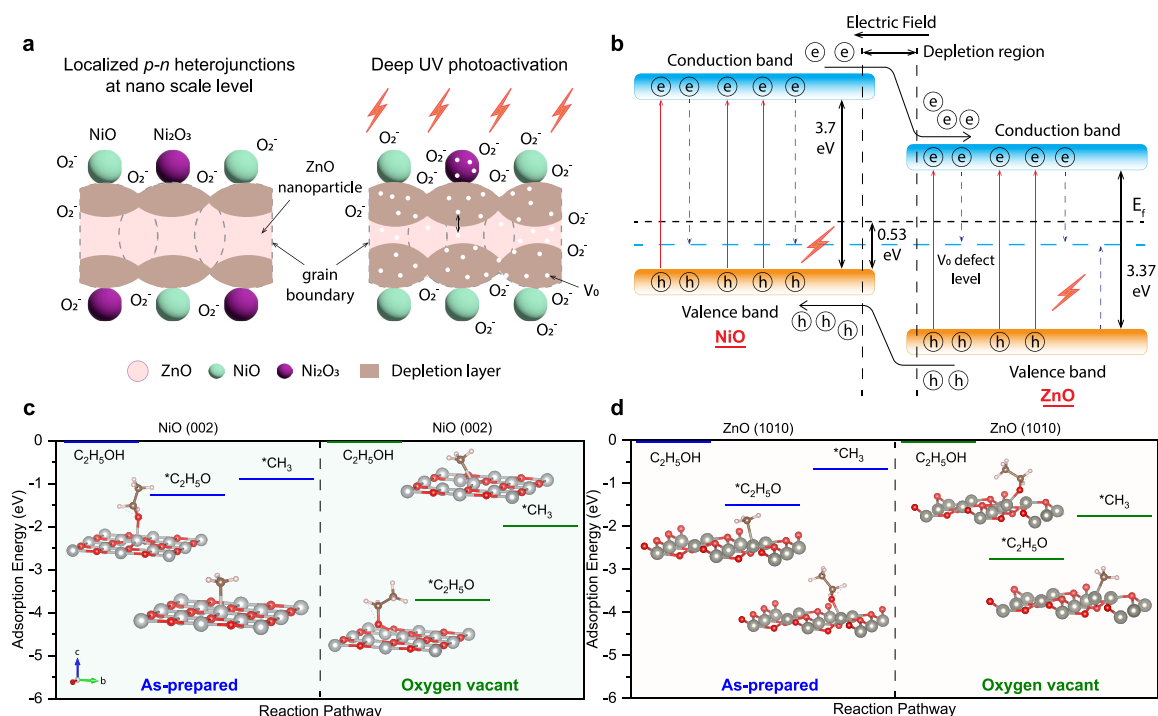[a]RT = room temperature. [b]I_{EtOH}/I_{air}.

Figure 1. Schematic illustration of (a) *p-n* nanoscale heterojunctions formed by the Ni_xO_y-ZnO nanoparticles and (b) their energy band diagram upon induction of the oxygen vacancies, showing the formation of an internal electric field at the nanoscale heterointerface with the vector pointing from positively charged *n*-ZnO to negatively charged *p*-Ni_xO_y. DFT calculations with corresponding geometric configurations of ethanol dissociation and adsorption on (c) as-prepared (without DUV photoactivation) and oxygen vacant (with DUV photoactivation) *p*-NiO (green shaded) and (d) *n*-ZnO (yellow shaded) surfaces with and without DUV photoactivation. The reaction pathway shows the physisorption of the ethanol molecule followed by its dissociation (chemisorption) into C_2H_5O and CH_3 by redox reactions on both surfaces.

potential role of the nanocomposite surface structure in enhancing surface interactions.

In parallel, semiconductor defect engineering, and in particular, induction of oxygen vacancies, has been explored to enhance the efficiency of various photocatalytic and photoelectrochemical processes,[15−17] including photoelectrochemical hydrogen production,[18] and organic photodecomposition.[19] Introducing oxygen vacancies in a semiconductor can

enhance the surface density of redox sites, increasing catalytic activity.[15,19,20] Zhang *et al.* optimized the chemical and electronic properties of NiO nanorods for electrocatalysis by oxygen vacancy engineering,[21] significantly enhancing the electrical conductivity and hydrogen evolution reaction kinetics. Li *et al.*[22] found that surface oxygen vacancies in ZnO nanofilms enhanced their photochemical sensing response to NO_2 gas molecules, with neutral oxygen and

doubly ionized oxygen vacancies favoring the adsorption of O_2 and NO_2 adsorption, respectively. Recently, defect engineering has been applied to enhance the electronic and photocatalytic properties of nanoscale heterojunctions, improving light harvesting,[15] charge separation and transfer,[23] and surface reaction kinetics.[15,24]

Despite this potential, current approaches for the induction of oxygen vacancies in nanoscale heterojunctions have significant limitations. Oxygen vacancies are often generated in heterostructures by doping, which requires relatively high temperatures and carefully controlled reaction environments (Table 1).[21] Most approaches also require postfabrication annealing. This makes it challenging to control the concentration of oxygen vacancies and provides limitations for the use of low-melting-temperature substrates. For instance, Li *et al.* introduced surface oxygen vacancies in ZnO nanofilms by annealing between 200 and 450 °C under UV light.[22] Xu *et al.* generated surface oxygen vacancies by Co doping of ZnO microspheres at 400 °C.[25] Hamedani *et al.* induced surface oxygen vacancies by doping CeO_2 in ZnO nanostructures under ultraviolet irradiation at 600 °C.[26] Furthermore, there is a lack of studies and approaches for the engineering of oxygen vacancies in *thick* porous films required to provide suitable surface area for many (photo)-electrocatalytic applications. Recently, Zhang *et al.* reported the ammonia sensing performance of dense films of oxygen-deficient ZnO-NiO nanoscale heterojunctions.[24] However, the low film porosity resulted in a relatively poor chemical sensing performance, with an ammonia limit of detection of 3000 ppm.

Here, we introduce a flexible approach for the engineering and fabrication of thick nanoscale heterojunction films with tailored surface and structural properties and excellent photochemical activity. Ultraporous nanoscale heterojunction networks of electron-depleted Ni_xO_y-ZnO nanoparticles were self-assembled by a scalable gas-phase approach. Oxygen defects were engineered in these Ni_xO_y-ZnO networks with a thickness of up to 10 μm *via* mild-temperature deep ultraviolet (DUV) photoactivation, as confirmed by X-ray photoelectron spectroscopy depth profiling. The induction of oxygen vacancies on the surface and throughout the nanoscale heterojunctions drastically increased their photocatalytic performance, resulting in a 30-fold enhancement of their photochemical sensing response to a representative gas analyte and a record-low limit of detection of 20 ppb at room temperature. The latter enhancement was explained by density functional theory (DFT) calculations, revealing an 80% increase in the analyte gas molecule adsorption energy upon oxygen vacancy induction. These insights provide an effective method to optimize the photocatalytic and optoelectronic properties of high-surface-area nanoscale heterojunction films with applications in a variety of emerging optoelectronic and photocatalytic devices.

RESULTS AND DISCUSSION

Figure 1a shows a schematic description of our approach for engineering the surface properties of thick nanoscale heterojunction films *via* DUV photoactivation under inert ambient conditions. Studies of surface oxygen vacancies in nanoscale heterojunction networks suggest that the formation of *p-n* nanoscale heterojunctions can increase surface band bending resulting in a larger surface depletion region,[34] which is beneficial to enhance the electrical transduction of both photo-[34] and chemical[35] interaction events. Furthermore, the

formation of localized midlevel electronic states, due to the presence of oxygen vacancies, can further increase the photoexcited charge separation efficiency, adding to the electrical field-based separation mechanism of nanoscale heterojunctions (Figure 1b).

We performed DFT modeling of the interaction of a representative analyte, ethanol, with the surface of pristine and oxygen vacant Ni_xO_y and ZnO surfaces (see Experimental Section). Figure 1c, d show that ethanol adsorbs on the pristine (as-prepared) and oxygen vacant Ni_xO_y and ZnO surfaces, respectively. The initial adsorption of ethanol on the surface is physisorption where ethanol molecules make contact with the metal oxide surfaces. Ethanol molecules adsorb on the ZnO surface and dissociate into intermediate components. There are various routes for ethanol disassociation on metal oxide surfaces and the associated charge carrier migration is quite intricate.[36] However, the proposed low-temperature physisorption and chemisorption processes are presented in Figure S1b.

After the ethanol adsorption, ethanol and the metal oxides participate in a redox reaction (chemisorption) and the ethanol molecule reduces to C_2H_5O (Figure S1b, Step 2). The C_2H_5O radicals have three isomers, ethoxy (CH_3CH_2O), 1-hydroxyethyl (CH_3CHOH), and 2-hydroxyethyl (CH_2CH_2OH) radicals.[37] These radicals play a pivotal role as reaction intermediates in the decomposition and combustion of ethanol. C_2H_5O can further decompose by 3 different reaction pathways; carbon−carbon bond fission, carbon−hydrogen bond fission, and isomerization followed by decomposition.[37,38] It has been reported in separate studies that the carbon−carbon bond fission (direct decomposition; Figure S1b, reaction path 1) is an order of magnitude faster than that of carbon−hydrogen bond fission and has the lowest reaction barrier as compared to reaction paths 2 and 3.[37,38] Our DFT calculations show higher adsorption energies of C_2H_5O on as-prepared Ni_xO_y (1.27 eV) and ZnO (1.51 eV), while for CH_3, it is 0.89 and 0.65 eV on the Ni_xO_y and ZnO surfaces, respectively, indicating the dominant decomposition pathway *via* reaction path 1. The induction of oxygen vacancies leads to a significant increase in the adsorption energy of C_2H_5O to 3.7 and 2.78 eV on the Ni_xO_y and ZnO surfaces, respectively. Similarly, the CH_3 adsorption energy increases to 2.0 and 1.78 eV on the oxygen vacant Ni_xO_y and ZnO surfaces, respectively (Figure 1d). This suggests that the induction of oxygen vacancies in the Ni_xO_y-ZnO nanoscale heterojunctions can increase the adsorption of ethanol gas molecules and facilitate their further reaction with the surface.

The higher adsorption energy on the Ni_xO_y is in line with its excellent surface activity,[39] making it one of the preferred *p*-type semiconductors for nanoheterojunction-based UV and photochemical sensing applications.[10,11] Recent models suggest that polycrystalline *p*-NiO has a strong ethanol sensing response at room temperature, due to enhanced electron transfer.[40] The high sensitivity and fast response to ethanol gas molecules of ZnO ($10\bar{1}0$) nanorods were attributed to the higher adsorption energies of ethanol, NH_3, H_2, CO, and O_2, computed by DFT calculations.[41] The latter was revealed to arise from an adsorption-induced reconstruction of the ($10\bar{1}0$) ZnO surface, which caused changes in the electronic structure. Similarly, Xu *et al.*[42] utilized DFT to explore the interactions of NO with the (110) surface of SnO_2, showing that the adsorption energy of NO on an oxygen-deficient surface is greater than on a stoichiometric one. It was also found that an
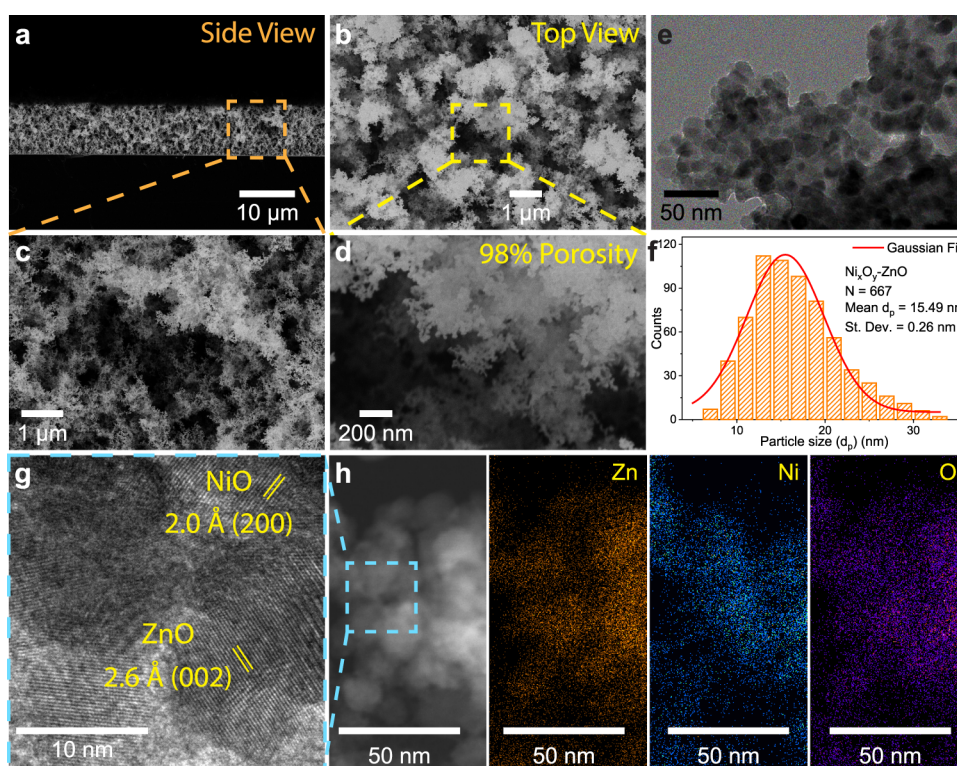
Figure 2. Low magnification scanning electron microscopic (SEM) images of the ultraporous Ni_xO_y-ZnO *p-n* nanoscale heterojunction networks: (a) cross-sectional and (b) top view. Corresponding high-resolution SEM images of (c) cross-sectional and (d) top view revealing high porosity in the nanoscale *p-n* heterojunction fractals. (e) Low-resolution transmission electron microscopic (TEM) image of Ni_xO_y-ZnO nanoscale *p-n* heterojunction networks and (f) Ni_xO_y-ZnO nanoparticle size analysis by TEM images showing an average size of 15.5 nm. (g) High-resolution TEM (HRTEM) of Ni_xO_y-ZnO nanoscale heterojunction networks showing the *d*-spacing of ZnO (2.6 Å), corresponding to (002) and NiO (2.0 Å), corresponding to (200) plane. (h) Backscattered TEM and the corresponding electron energy-dispersive X-ray spectroscopy (EDS) elemental mapping of Ni_xO_y-ZnO nanoscale heterojunction networks.

oxygen-deficient surface with physisorbed oxygen exhibits a further increase in the interaction with NO. The importance of the surface's stoichiometry, including the presence of oxygen vacancies, was further corroborated by other studies.[43] Here, we proposed that the oxygen vacancies induced by DUV irradiation improve the charge separation efficiency, increase the depletion region, and enhance charge transfer rates between the analyte molecule and the nanoscale heterojunction networks, thereby promoting the analyte adsorption and dissociation on the metal oxide surfaces and at the nanoscale heterojunction networks with significantly high adsorption energies.

In addition to the surface properties, the photochemiresistive performance of nanoscale heterojunctions depends on the porosity and thickness of the layer. Here, 98% porous networks of ZnO nanoparticles with a thickness of 10 μm were self-assembled by flame spray pyrolysis (FSP) (Figure S1a) and decorated by Ni sputtering and postsintering (see Experimental Section), as previously reported.[11] A low magnification cross-sectional scanning electron microscopic (SEM) image of the Ni_xO_y-ZnO nanoscale heterojunction networks reveals their uniform thickness (8−10 μm) across the substrate, with no cracks or visible defects (Figure 2a). Aerosol deposition allows precise control over the network thickness, porosity, and average nanoparticle size, resulting in highly pure ZnO films.[10,44] Here, thickness (8−10 μm) and porosity (~98%) were obtained by controlling the flame exposure time and the height above the burner, which were optimized at 100 s and 20 cm, respectively.

For the first time, oxygen vacancies were induced in these nanoscale heterojunction networks by DUV photoactivation at 200 °C using an excimer lamp (30 mW cm^{-2}) in a nitrogen atmosphere. The short-wavelength and high-energy DUV irradiation (172 nm and 7.2 eV) were effective for deep penetration of DUV light into the ultraporous network morphology at a low temperature. This enabled the creation of oxygen vacancies not only on the surface but also several micrometers below the top surface while preserving the integrity of nanoscale heterojunction networks. Figure 2b presents a low magnification top-view SEM image of the Ni_xO_y-ZnO nanoscale heterojunction networks. The corresponding high magnification SEM images (Figure 2c,d) reveal the presence of 1−4 μm macro- and 500 nm mesopores, in line with metal oxide nanoparticle networks previously synthesized *via* the flame-aerosol route.[44,45]

SEM images at various magnifications show a self-similar fractal structure (Figure S2) with a porosity of *ca.* 98% (Experimental Section). These Ni_xO_y-ZnO fractals were analyzed for their fractal dimensions and lacunarity. The fractal dimension, D_f, is a dimensionless number that represents the complexity and self-similarity of a fractal system, usually ranging from 1.75 to 2.5 for aerosol-deposited materials. It can be measured using scattering techniques such as light, X-ray, and neutron scattering, or image analysis.[45] Figure 2c was used to calculate the D_f and lacunarity of Ni_xO_y-ZnO fractals using image analysis and the fractal image generated by pixel distribution is presented in Figure S2c (see Experimental Section). Here, a fractal dimension of 1.81 ±
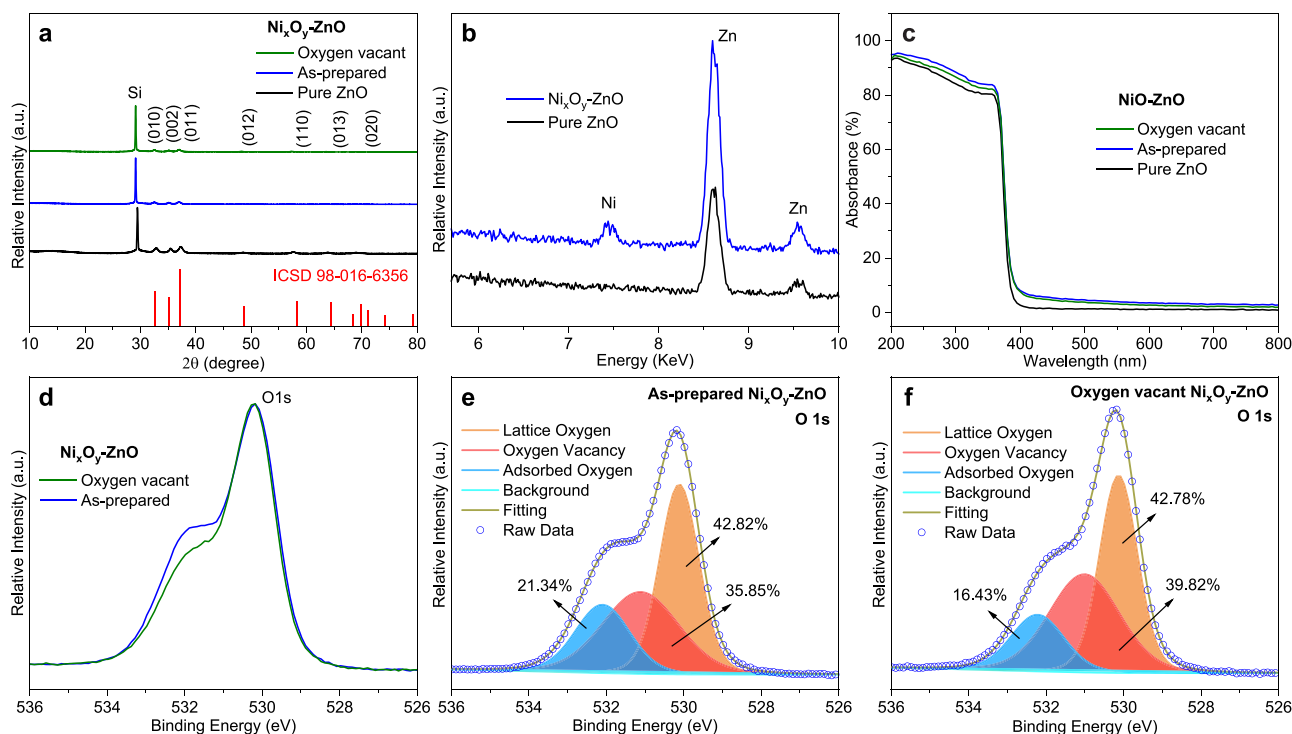
Figure 3. X-ray diffraction (XRD) patterns of (a) Ni_xO_y-ZnO nanoscale heterojunction networks with pure ZnO and the reference patterns. (b) Energy dispersive spectra (EDS) of Ni_xO_y-ZnO nanoscale heterojunction networks. (c) Optical absorbance. (d) High-resolution O 1s X-ray photoelectron spectroscopy (XPS) spectra of Ni_xO_y-ZnO nanoscale heterojunction networks. Deconvoluted O 1s spectra of (e) as-prepared and (f) oxygen vacant Ni_xO_y-ZnO nanoscale heterojunction networks.

0.04 was computed for these Ni_xO_y-ZnO nanoscale heterojunction networks using the image processing and box-counting algorithms (see Experimental Section), as visualized in the slope of ln N versus ln ε plot in Figure S3a. The lacunarity, Λ, quantifies the inhomogeneity of fractal structures and was calculated from the variance, σ, and the mean, μ, of the foreground pixel distribution (Figure S2c). The plot of the lacunarity versus box length in Figure S3b shows the maximum between 0 and 0.4 μm (0−400 nm), indicating a higher degree of inhomogeneity and uniform disorder on this length scale. These values are in line with previous reports on flame-aerosol-made films and a layer porosity of 98%.[45,46]

The compositional and morphological configuration of the localized Ni_xO_y-ZnO nanoscale heterojunction networks were studied using transmission electron microscopy (TEM). The nanoparticles were found to be quasi-spherical (Figure 2e) with a mean particle diameter, d_p, of 15.5 ± 0.26 nm, estimated by measuring 667 nanoparticles (Figure 2f) with an estimated specific surface area of ZnO base sensing layer to be 690 m²/g (Text S1). High-resolution TEM (HRTEM) revealed a d-spacing of 2.6 Å corresponding to the (002) plane of ZnO and 2.0 Å corresponding to the (200) plane of NiO (Figure 2g).[24] Backscattered TEM and electron energy-dispersive X-ray spectroscopy (EDS) elemental mapping analyses were also conducted to confirm the presence and morphology of Ni_xO_y on the ZnO nanoparticle networks (Figure 2h). Figure 2g−h reveal that the Ni_xO_y nanoparticles were in close contact with the ZnO nanoparticles forming a network of nanoscale heterojunctions. The analysis in Figure 2h also suggests a uniform distribution of Ni_xO_y in the ZnO nanoparticle network.

X-ray diffraction (XRD) analysis shows a highly crystalline nature and purity of the nanoscale heterojunction networks.

The XRD patterns of pure ZnO, as-prepared Ni_xO_y-ZnO, and oxygen vacant Ni_xO_y-ZnO are shown in Figure 3a. All of the peaks match the reference pattern of zincite (ICSD 98−016−6356) with a hexagonal crystal system and the space group of P63mc. No Ni peaks were found in the XRD patterns of both the as-prepared and the oxygen vacant Ni_xO_y-ZnO networks. This was attributed to the low content of Ni as compared to the ZnO nanoparticles. The average crystal sizes for the as-prepared and oxygen vacant Ni_xO_y-ZnO nanoscale heterojunction networks were 11.7 ± 2.1 nm and 11.8 ± 2.0 nm.[47] These results align with the average d_p of 15.5 nm calculated by TEM analysis, indicating the presence of mostly single-crystal nanoparticles. These results also show that the DUV photoactivation did not affect the grain size of the metal oxide nanoscale heterojunction networks, making them suitable for catalysis and detection applications.

To confirm the composition of the sputtered Ni_xO_y, pure Ni_xO_y films were made with the same conditions and analyzed using Grazing Incidence XRD (GI-XRD) with an incident angle of 5 degrees and step size of 0.052 degrees (Figure S4a). The peaks matched the reference pattern of Bunsenite (ICSD 98−002−4014) with a cubic crystal system and the $Fm\overline{3}m$ space group. Subsequently, the Ni_xO_y-ZnO nanoscale heterojunction networks were also analyzed using GI-XRD at an incident angle of 3° with a step size of 0.11°. However, as in the case of the standard XRD analysis, the key peak of NiO at ~43° was not detected (Figure S4b). This is due to the finer distribution of the Ni_xO_y nanoparticles in the highly porous ZnO nanoparticle networks, which lead to very small Ni_xO_y crystal sizes.

To further ascertain the presence of Ni_xO_y, EDS analysis was performed for the pure ZnO and Ni_xO_y-ZnO networks. The EDS spectra of Ni_xO_y-ZnO show peaks for both Ni (7.4 K eV)
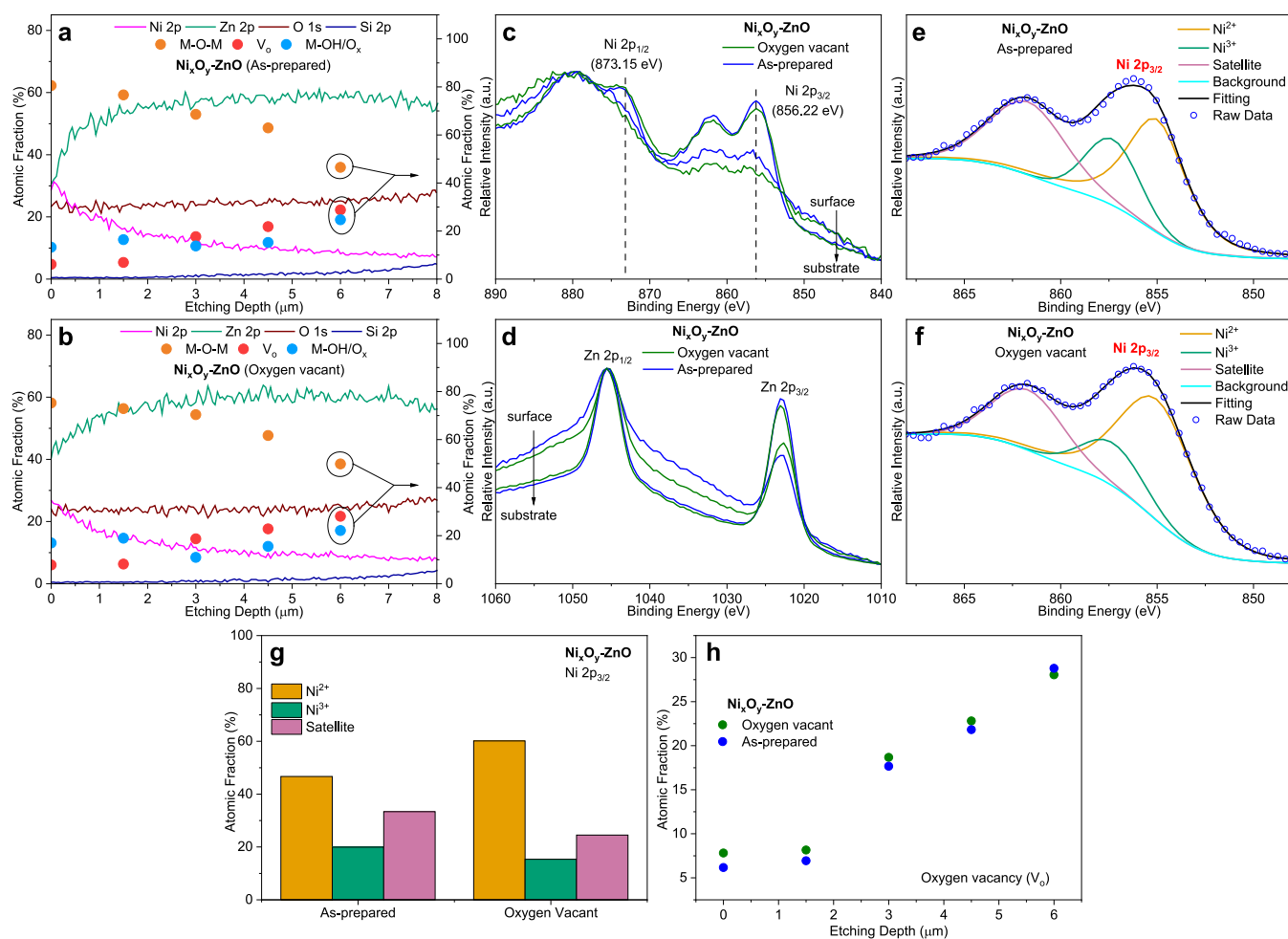
Figure 4. XPS depth profiles as a function of the ion etching depths of (a) as-prepared and (b) oxygen vacant Ni_xO_y-ZnO nanoscale heterojunction networks showing the fractions of oxygen (brown line), Zn (green line), Ni (pink line), Si (blue line), M-O-M (orange circle), V_o (red circle), and M-OH/O_X (blue circle) content. High-resolution XPS spectra of the as-prepared and oxygen vacant Ni_xO_y-ZnO nanoscale heterojunction networks at various depths showing the (c) Ni 2p and (d) Zn 2p. Deconvoluted Ni 2p spectra of (e) as-prepared and (f) oxygen vacant Ni_xO_y-ZnO nanoscale heterojunction networks. Atomic fractions of (g) Ni^{2+} and Ni^{3+} and (h) oxygen vacancies in as-prepared and oxygen vacant Ni_xO_y-ZnO nanoscale heterojunction networks.

and Zn, while no Ni peaks were observed for the pure ZnO layers (Figure 3b). This confirms the successful deposition of Ni_xO_y on the ultraporous ZnO nanoparticle networks. UV−vis analysis was conducted to examine the optical properties of the films after Ni deposition and DUV photoactivation. Figure 3c displays the optical absorbance of the pure ZnO and of the as-prepared and oxygen vacant Ni_xO_y-ZnO nanoscale heterojunction networks. The absorbance of all films decreases at a wavelength of *ca.* 375 nm, which corresponds to the direct band gap of ZnO (3.35 eV). An optical band gap (E_g) of 3.28 eV was estimated by the Tauc plot for all of the nanoparticle networks (Figure S4c). The optical analysis of the heterostructures shows that there was no change in the optical properties of the films after Ni deposition or after the generation of oxygen vacancies *via* DUV photoactivation.

X-ray photoelectron spectroscopy (XPS) was used to analyze the changes in the composition and state of the Ni_xO_y-ZnO nanoscale heterojunction networks after DUV. Depth profiling was conducted to examine the distribution of oxygen vacancies and the valence state of metal ions throughout the cross-section of the nanoscale heterojunction networks. XPS scans were recorded after layer-by-layer Ar ion

etching. Only Zn, Ni, O, and Si (from the substrate) were detected (see Experimental Section). The absence of other peaks reveals a high purity of the films made by flame-aerosol deposition. All binding energies were corrected by using the adsorbed carbon dioxide peak as a reference in the carbon 1s (C 1s) spectra.[48] The XPS survey spectra of Ni_xO_y-ZnO nanoscale heterojunction networks before and after the DUV photoactivation are shown in Figure S5a. Figure 3d−f present the high-resolution O 1s spectra of the top surface of both the as-prepared and oxygen vacant Ni_xO_y-ZnO nanoscale heterojunction networks. The fraction of oxygen defects increased by 10.5% after DUV photoactivation, and the fraction of loosely bound surface oxygen groups decreased by 26% (Figure 3e, f). A summary of the XPS characteristics in the O 1s of the as-prepared and oxygen vacant Ni_xO_y-ZnO nanoscale heterojunction networks is given in Table S1.

The results of the XPS depth profiling are shown in Figure 4a and b before and after DUV photoactivation, respectively. The complete depth profiles of the elements detected in Figure S5b-c show a decrease in metal peaks and an increase in the Si (substrate) peak with increasing etching depth and thus proximity to the Si substrate. More in detail, the rise in the O
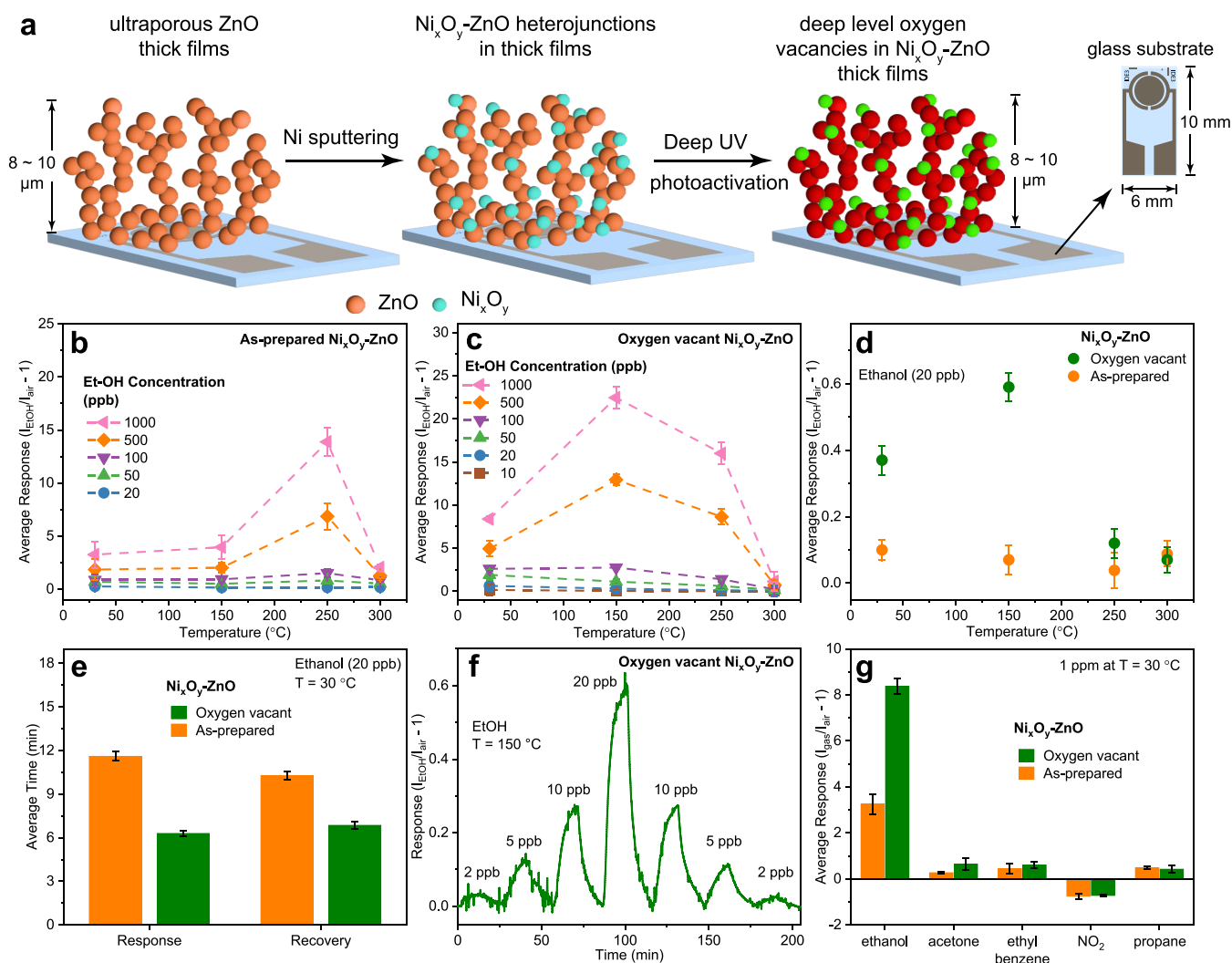
Figure 5. (a) Schematic of the photochemoresistive sensor fabrication. Average ethanol sensor response as a function of concentration and temperature of (b) as-prepared and (c) oxygen vacant Ni_xO_y-ZnO. (d) The average sensor response to 20 ppb ethanol as a function of temperature. (e) Average response and recovery times of the as-prepared and oxygen vacant Ni_xO_y-ZnO to 20 ppb ethanol at room temperature. (f) Representative sensor response dynamic of the oxygen vacant Ni_xO_y-ZnO nanoscale heterojunction networks to low concentration (2−20 ppb) of ethanol at the optimal temperature of 150 °C. (g) Selectivity of the as-prepared and oxygen vacant Ni_xO_y-ZnO nanoscale heterojunction networks to 1 ppm of propane, NO_2, ethylbenzene, acetone, and ethanol at room temperature.

1s signal intensity is due to the contribution of oxygen from the native oxide of the SiO_2 substrate. The O 1s spectra were deconvoluted into three peaks by a Gaussian−Lorentzian function to determine the fraction of oxygen vacancies. These peaks represent lattice oxygen groups (530.25 ± 0.2 eV, M-O-M), oxygen defects (531.05 ± 0.2 eV, V_o) in ZnO and Ni_xO_y, and loosely bound oxygen groups (532.19 ± 0.2 eV, M−OH/ O_x) such as hydroxyl groups or oxygen molecules adsorbed on the Ni_xO_y-ZnO nanoscale heterojunction networks (Figure S6).[3,21,49] Table S2 shows the calculated values of each oxygen species with and without DUV photoactivation at various depths of the nanoscale heterojunction networks. High-resolution spectra of O 1s, Zn 2p, and Ni 2p at all etching levels are provided in Figure S7.

Despite the significant thickness of the ZnO nanoparticle networks and the line-of-sight nature of the sputtering process, the presence of Ni was observed throughout the whole cross-section of the nanoscale heterojunction networks. This is attributed to the highly porous fractal structure of the aerosol self-assembled ZnO nanoparticle networks that allowed Ni to penetrate deeply into the nanoparticle networks, creating localized p-n nanoscale heterojunction networks of Ni_xO_y-ZnO (Figure 4c). The composition of the deposited Ni was also uniform throughout the cross-section, with the Ni 2p spectra showing a consistent split into $2p_{1/2}$ and $2p_{3/2}$ both near the top surface of the network and close to the substrate (Figure 4c).

Figure 4d displays high-resolution Zn 2p spectra of the as-prepared and oxygen vacant nanoscale heterojunction networks. Both spectra show two peaks in Zn 2p spectra due to spin−orbital coupling, which are $2p_{1/2}$ and $2p_{3/2}$, respectively. There was no peak shift in the oxygen vacant nanoscale heterojunction networks, obtained by DUV exposure. This excludes the substitutional replacement of Ni in the Zn sites, which would impact the bonding energy of the local Zn atoms. This was also confirmed by XRD (Figure 3a−c) indicating that the sputtered Ni atoms did not dope in the ZnO crystal lattice but formed segregated domains. The relative increase in the intensity of Zn 2p with increasing etching depth is attributed to the lesser amount of Ni penetrating close to the substrate. The

Ni $2p_{3/2}$ spectra of Ni_xO_y-ZnO nanoscale heterojunction networks were deconvoluted into three peaks by using a Gaussian−Lorentzian function. These peaks confirmed the presence of two valence states of Ni: Ni^{2+} around 854.5 eV and Ni^{3+} around 857.8 eV. The deconvoluted Ni $2p_{3/2}$ spectra of the as-prepared and oxygen vacant Ni_xO_y-ZnO nanoscale heterojunction networks are shown in Figure 4e, f. The results show that NiO is the dominant nickel oxide phase in the as-prepared nanoparticle networks, while a minor amount of Ni_2O_3 was also present. DUV photoactivation further decreased the fraction of Ni^{3+} (Figure 4g), in line with the induction of oxygen vacancies in the nanoscale heterojunction networks. The fraction of oxygen defects at various depths of the heterostructures increased as a result of UV exposure, as seen in Figure 4h.

To investigate the impact of the oxygen vacancy on the photocatalytic activity and electrical properties of the nanoscale heterojunction networks, chemical sensors were fabricated on commercial Pt interdigitated electrode substrates (Experimental Section) by the same flame-aerosol self-assembly (Figure 5a), with the same ZnO thickness and Ni-loading as shown in the above characterizations. The thickness of the ZnO layer was selected in line with previously best-performing chemical sensors and UV-photodetectors.[10,11,50] Ethanol was used as a test analyte to interrogate the photochemoresistive properties of the Ni_xO_y-ZnO nanoscale heterojunction networks before and after the induction of oxygen vacancies. The sensor response was measured as a change in current at a constant voltage of 1 V. All the sensors were constantly exposed to synthetic air and solar illumination (AM1.5 solar simulator, 67 mW cm^{-2}) while cycling the exposure to the analyte gas on/off during 15 min cycles. The sensing experiments were performed three times at temperatures between 30 and 300 °C with ethanol concentrations ranging from 10 to 1000 ppb. The average response was reported with the standard error as an error bar.

The representative dynamic response of the as-prepared and oxygen vacant Ni_xO_y-ZnO nanoscale heterojunction networks to ethanol concentrations between 10 ppb and 1 ppm are shown in Figure S8a, b. The sensor response increased with an increasing ethanol concentration. Notably, the sensors were able to detect very low concentrations of ethanol at low temperatures (30−150 °C). However, the as-prepared Ni_xO_y-ZnO nanoscale heterojunction networks could not detect 10 ppb of ethanol at any temperature, while the oxygen vacant Ni_xO_y-ZnO nanoscale heterojunction networks achieved the detection of 10 ppb of ethanol already at room temperature (Figure S8a, b). Furthermore, Figure 5b, c shows that the induction of oxygen vacancies decreased the optimal sensor operating temperature from 250 to 150 °C and significantly increased the sensor response. At room temperature, the sensor response to 1 ppm of ethanol increases by 88% and by 140% at 150 °C.

The response to the trace concentration (20 ppb) of ethanol also increases by 83% at room temperature (Figure 5d). Furthermore, the response and recovery times to 20 ppb ethanol at room temperature decrease by 59% and 40% after DUV photoactivation (Figure 5e). Notably, the oxygen vacant Ni_xO_y-ZnO nanoscale heterojunction networks show a better response at lower temperatures as compared to the as-prepared Ni_xO_y-ZnO nanoscale heterojunction networks. However, at high temperatures, the response decreases. This is attributed to the oxygen vacancies becoming more mobile and the nanoscale

heterojunctions becoming more catalytically active, causing the combustion of ethanol molecules before they reach the most sensitive bottom part of the nanoscale heterojunction networks near the interdigitated electrodes as suggested for other highly catalytic active chemoresistive films.[51] To assess the long-term stability of oxygen vacant Ni_xO_y-ZnO nanoscale heterojunction networks, the sensors were tested after one month of initial experiments at 150 °C. A decrease of 159% was observed for 1 ppm of ethanol at 150 °C (Figure S9a). Furthermore, the ethanol testing was carried out with oxygen vacant Ni_xO_y-ZnO sensors in realistic conditions for the possible application as breath analyzers in relative humidity of 30 and 50% at room temperature under dark conditions (Figure S9b). The sensors did not respond to any concentration of ethanol gas. This was attributed to the lower number of reaction sites available to the ethanol in the presence of an interfering gas such as H_2O molecules, a low operating temperature of the sensors as well as the absence of solar light.

Overall, the above characterization shows that the generation of oxygen vacancies significantly improves the sensitivity, lowers the detection limit, and improves the response and recovery times of the Ni_xO_y-ZnO nanoscale heterojunction networks enabling their operation at lower temperatures. Notably, our nanoscale heterojunction networks achieve the highest responsivity reported among recently reported sensors based on nano heterostructures with oxygen defects (Table 1). It should also be noted that, here, the oxygen vacancies in the Ni_xO_y-ZnO nanoscale heterojunction networks were effectively generated using our cost-effective low-power (30 mW cm^{-2}) DUV photoactivation process at 200 °C, compared to other expensive, multistep, and high-temperature methods which may damage and/or compromise the stability of the fragile nanoscale heterostructure networks.

Ni_xO_y-ZnO nanoscale heterojunction networks with oxygen vacancies showed a very low limit of detection of 2 ppb of ethanol at 150 °C. Figure 5f shows the dynamic sensor response to extremely low concentrations of ethanol (2−20 ppb) at this optimal temperature (150 °C). Furthermore, poor selectivity at low temperatures is a drawback of metal oxide sensors. Here, the oxygen vacant Ni_xO_y-ZnO nanoscale heterojunction networks displayed excellent selectivity for ethanol close to room temperature (30 °C) against other volatile organic compounds (VOCs) (Figure 5g). Notably, the ethanol selectivity increased 30 times after DUV photoactivation. The latter led to no significant improvement in the response to propane and NO_2 gases, while an increase in the response toward acetone and ethylbenzene was observed at room temperature. This difference in the response was tentatively attributed to the differences in the polarity and size of these VOC molecules. Generally, ethanol molecules show higher binding affinities as the bipolar hydroxyl group (OH) interacts with the surface via two different charge transfer mechanisms, unlike monopolar molecules like acetone. This has been reported recently for SnO_2 at room temperature and confirmed both experimentally and theoretically.[52] Notably, both as-prepared and oxygen vacant Ni_xO_y-ZnO nanoscale heterojunction networks also showed an inverse response to NO_2 gas as expected for oxidizing analyte and p-type semiconductors (Figure 5g).

To confirm this mechanism and gain further insights into the role of the oxygen vacancy in enhancing the response and selectivity to ethanol, DFT calculations were carried out to study the effects of surface adsorption and decomposition of
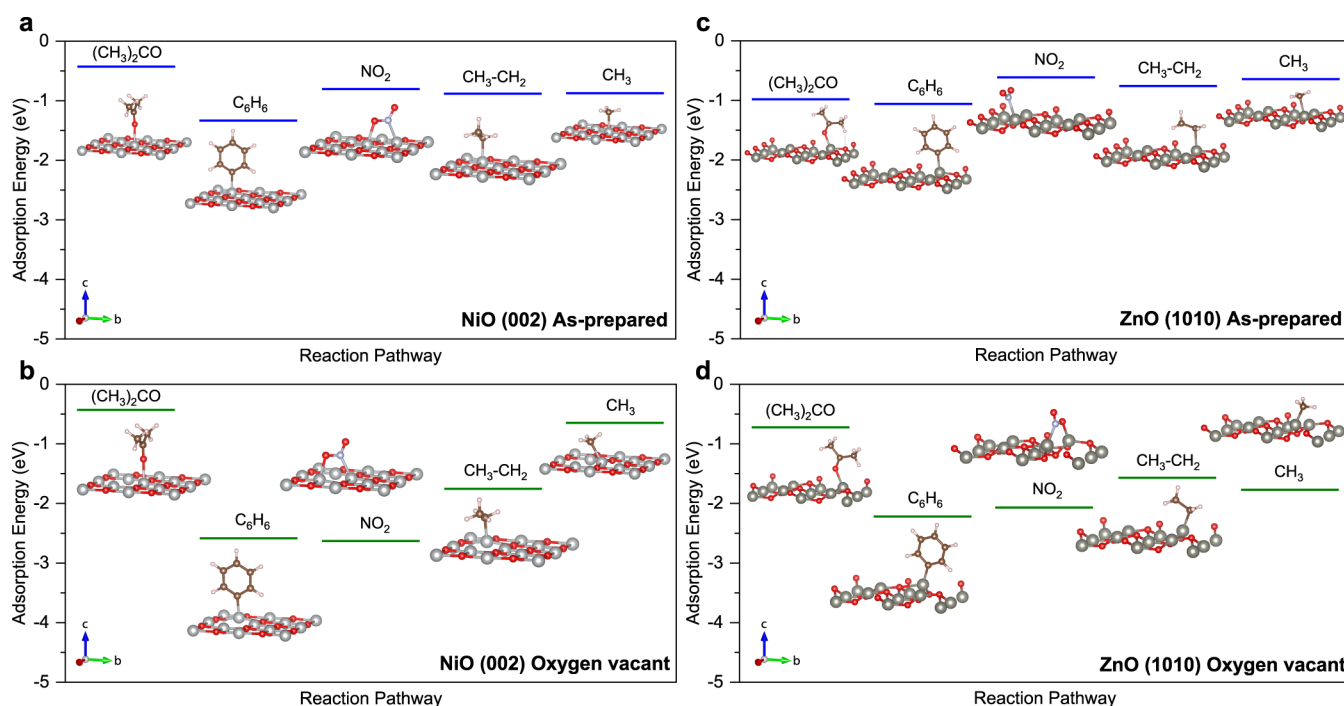
Figure 6. Adsorption energies of various VOCs with corresponding geometric configurations calculated by theoretical analysis using DFT of NiO (a) as-prepared and (b) oxygen vacant and of ZnO (c) as-prepared and (d) oxygen vacant.

VOCs on the p-type NiO and n-type ZnO surfaces with and without DUV photoactivation. The preferential planes of (002) and (10$\bar{1}$0) were selected for NiO and ZnO nanoparticle networks with cubic and hexagonal crystal structures, respectively. Geometrical optimizations were achieved by relaxing all ionic positions and supercell vectors until the Hellman-Feynmann forces were less than 0.02 eV^{-1}. The dispersion correction was also considered in this study by using the DFT-D3 method.[53] The slab method was used to model NiO and ZnO surfaces with surface-bulk-like interactions by fixing the coordinates of the atoms in three bottom layers and relaxing the coordinates of the atoms in the three uppermost layers. The results show that all VOC molecules dissociate at the surface of the nanoparticles and that the corresponding adsorption energies increase in the presence of oxygen vacancies (Figure 6a−d).

The dissociation of VOC molecules can occur through diverse pathways that involve intricate reaction kinetics. In particular, ethylbenzene (C_8H_{10}) molecules can undergo direct reactions with the sensing layer to produce a response signal, or they can decompose into C_6H_6, C_3H_8, or CH_3. The adsorption energy of NO_2 molecules on p-type NiO increased from 0.8 to 2.6 eV, while that on n-ZnO rose from 0.6 to 2.1 eV after the introduction of oxygen vacancies. This resulted in a cumulative increase of 108% in the adsorption energy of NO_2 molecules in Ni_xO_y-ZnO nanoscale heterojunction networks due to oxygen vacancies. Notably, the rise in the adsorption energies of NO_2 molecules was more significant in n-type ZnO compared to p-type NiO. However, the increase was highest in the case of ethanol molecules. Furthermore, this increase in ethanol adsorption energy was higher (∼98%) in the p-type NiO as compared to n-type ZnO (∼59%). This indicates that the formation of p-n Ni_xO_y-ZnO nanoscale heterojunction networks and the presence of oxygen vacancies in both metal oxides can be used to enhance the selectivity of metal oxide gas sensors by surface energy engineering. The adsorption energies

for different VOCs on both as-prepared and oxygen vacant Ni_xO_y-ZnO nanoscale heterojunction networks are summarized in Table 2.

Table 2. Summary of Adsorption Energies of Various VOCs on As-Prepared and Oxygen Vacant Ni_xO_y-ZnO Nanoscale Heterojunction Networks

VOC Species	As-prepared NiO(002)	Oxygen vacant NiO(002)	As-prepared ZnO(10$\bar{1}$0)	Oxygen vacant ZnO(10$\bar{1}$0)
$(CH_3)_2CO$ (acetone)	−0.43	−0.42	−0.99	−0.74
C_2H_5O (from C_2H_5OH-ethanol)	−1.27	−3.69	−1.51	−2.78
Benzene (from C_8H_{10}-ethylbenzene)	−1.35	−2.59	−1.07	−2.23
NO_2 (Nitrogen dioxide)	−0.82	−2.64	−0.60	−2.07
CH_3−CH_2 (from C_3H_8-propane or ethylbenzene)	−0.91	−1.75	−0.75	−1.57
CH_3 (from propane, acetone, ethylbenzene, ethanol)	−0.89	−2.00	−0.65	−1.78

Given the above experimental characterization and modeling results, here, we attribute the strong increase in the photochemoresistive sensor performance to a higher photocatalytic activity of the surface due to the formation of oxygen vacancies in both Ni_xO_y and ZnO and the localized p-n nanoscale heterojunctions between Ni_xO_y and ZnO that facilitate the photoexcited charge separation making them available for the interaction with the analyte molecules. Furthermore, the ultraporous morphology of the electron-depleted (d_p < Debye length) Ni_xO_y-ZnO nanoscale heterojunction networks facilitate the diffusion of the analyte gas and products in and out of the sensing element resulting in

an increased active area. At ambient conditions, oxygen adsorbs on the surfaces of Ni_xO_y and ZnO and traps electrons, forming O_2^-, and increasing the depletion region[19,24] (Figure S10 and 1a). The mismatch between the bandgap and Fermi level causes electrons to flow from Ni_xO_y to ZnO and holes flow in the opposite direction at Ni_xO_y-ZnO nanoscale heterojunctions, effectively separating electrons, and holes (Figure 1b). The photocharge separation at the Ni_xO_y and ZnO also allows for charges to be available on the ZnO and Ni_xO_y surface leading to, respectively, more and less oxygen chemisorption, increasing the number of reaction sites available for target gas molecule, such as ethanol on the surface of the nanoscale heterostructures.

CONCLUSION

In summary, we have reported a flexible approach for the engineering of the surface activity of high-performance three-dimensional nanoscale heterojunction networks, demonstrating vastly enhanced photoactivity and sensing performance. Ultraporous nanoparticle networks of Ni_xO_y-ZnO nanoscale heterojunctions were self-assembled by flame-aerosol deposition and sputtering leading to highly uniform, electron-depleted porous layers. Oxygen vacancies were induced throughout the whole Ni_xO_y-ZnO nanoscale heterojunction networks in a controllable manner by a moderate temperature deep UV photoactivation. XPS depth profiling showed the presence of localized p-n nanoscale heterojunctions and oxygen vacancies throughout the Ni_xO_y-ZnO whole 8−10 μm thick networks. Upon induction of oxygen vacancies, the sensing performance of the nanoscale heterojunction networks increased substantially. The sensitivity to ethanol, as a representative analyte, was enhanced by 88% with a detection limit of 2 ppb at 150 °C and a 30-fold increase in selectivity against a panel of other VOCs at room temperature. Theoretical study of the as-prepared and oxygen vacant nanoscale heterojunction surface by DFT revealed that the adsorption energy of ethanol increased by 80% in the oxygen vacant Ni_xO_y-ZnO nanoscale heterojunction networks, explaining the strong increase in photochemoresistive response of the DUV photoactivated devices. Overall, the high specific surface area, efficient separation of electron−hole pairs at the nanoheterojunction interfaces, deep penetration of target gas molecules into the porous networks, and oxygen-vacant surface all contributed to the outstanding performance of this nanoscale architecture, achieving record-high sensitivity and selectivity at room and moderated temperatures. We believe that these findings provide a facile approach for the engineering of highly performing photocatalytic materials with applications including miniaturized sensing, photocatalysis, and a variety of optoelectronic applications.

EXPERIMENTAL SECTION

Materials. All materials were used as received without any further purification. Zinc naphthenate (10% Zn, Merck) was used as a precursor and dissolved in xylene (Merck) to generate a solution with a total Zn metal atom concentration of 0.3 M. The solution was stirred for 30 min at room temperature to ensure complete dispersion.

Fabrication of Ni_xO_y-ZnO. Flame spray pyrolysis (FSP) was used to synthesize and for direct deposition of ZnO nanoparticles on Pt-interdigitated electrodes.[44,45] The Zn precursor solution was delivered via an automatic syringe pump (New Era syringe pump; Model: NE-300) at a flow rate of 5 mL min⁻¹ and dispersed into a fine spray with 7 L min⁻¹ oxygen at a constant pressure drop of 4.5 bar. The spray was ignited by supporting premixed methane/oxygen flames (CH_2 =

1.8 L min⁻¹, and O_2 = 2 L min⁻¹). Glass substrates containing 180 pairs of Pt interdigitated electrodes of 5 μm width and spacing (Micrux, Spain) were placed on a water-cooled substrate holder at a height above burner (HAB) of 20 cm. All substrates were cleaned three times with ethanol before deposition. After FSP deposition, the substrates were heat-treated at 300 °C for 12 h in a furnace (Brother High-Temperature Furnace XD-1.2KN) to stabilize the nanoparticle size and avoid resistive sintering during the gas sensing measurements. Ni was deposited by an AJA ATC 2400 magnetron sputtering system in an ambient Ar/O_2 chamber (18/2 sccm). The chamber was evacuated to 9×10^{-7} Torr before deposition and sputtering deposition was performed at a gas pressure of 4×10^{-3} Torr for 45 s at room temperature with a power of 200 W. The equivalent of a 6 nm Ni layer bulk thickness was sputtered onto these ultraporous ZnO nanoparticle networks and thereafter sintered at 300 °C for 12 h to form localized Ni_xO_y-ZnO p-n nanoscale heterojunctions and improve interparticle necking and connectivity.

For the DUV photoactivated modulation of FSP-synthesized ZnO films, a customized temperature-controllable system was adopted for precise temperature control, and a homemade DUV irradiation system was designed by using an excimer lamp (UV emission wavelength of 172 nm, 20×12 cm², Wonik Q & C) with the constant intensity of UV ~ 30 mW cm⁻². Dry N_2 gas was supplied to the customized chamber to prevent the formation of ozone (O_3) and the films and sensor devices were identically heated at 200 °C for 2 h under UV.

Material Characterization. Topographical and optical characterization techniques were used to analyze the morphology of the samples. Analytical scanning electron microscopy, (Zeiss Ultra plus field emission scanning electron microscope (FESEM)) was used for morphological analysis at 3 kV. The results were analyzed using ImageJ software and the FracLac plugin to calculate the fractal dimensions and lacunarity.[45,54] This algorithm covers the SEM image of the analyzed object with a grid of decreasing dimensionality and counts the number of boxes required to fully capture the solid image. In this way, the structure of the pattern is captured with a high accuracy. Information about the morphology, particle size, and lattice plane spacing was acquired by using a high-resolution transmission electron microscope (JEOL 2100F HRTEM) operated at 200 kV. A small amount of powder sample was added to ethanol and sonicated for 20 min to achieve a stable suspension, followed by casting a drop onto Lacey carbon 200 mesh nickel grids. The particle size distribution was evaluated by manually measuring the size of 625 nanoparticles using ImageJ. The simulation of the polycrystalline TEM diffraction patterns was performed using the JEMS[55] code as implemented on version 4.6131U2018. A Bruker D2 Phaser diffractometer was utilized to perform X-ray diffraction (XRD). Each sample was scanned using a Cu Kα (1.54) radiation source with an operating voltage of 30 kV and a current of 10 mA. The XRD patterns were recorded with a scan rate of 0.75° min⁻¹ in the 2θ range of 10−80° at an increment of 0.02°. The modified Scherrer equation[47] was applied to accurately calculate the crystalline domain size. XRD patterns were analyzed by commercially available software HighScore Plus using the Inorganic Crystal Structure Database (ICSD). The modified Scherrer equation is used to accurately estimate the size of nanoparticles from XRD peaks[47] and is given by

$$\ln \beta = \ln \frac{1}{\cos \theta} + \ln \frac{K\lambda}{D} \qquad (1)$$

where β is full width at half-maximum, in radians, located at any 2θ position in the pattern, λ (nm) is the radiation of wavelength, K is the Scherrer constant or shape factor, and D is the particle size in nm.

XRD data were recorded at room temperature on a PANalytical Empyrean Series 1 diffractometer fitted with a 1D PIXcel detector. Standard Bragg−Brentano data collections utilized fixed diversion slits in the incident beam and a Ni filter to remove Cu Kβ radiation to achieve Cu Kα$_I$ and Cu Kα$_{II}$ radiation source. Grazing incident experiments (GI-XRD) utilized a hybrid monochromator to achieve a parallel Cu Kα radiation source; the incident angle is reported with the data.

UV−Vis transmittance and absorption spectra were measured using a PerkinElmer (Lambda 1050 UV/vis/NIR) spectrophotometer. The characterization for both atomic orbital and chemical composition was analyzed by X-ray photoelectron spectroscopy (XPS, K-APLPHA +, Thermo Fisher Scientific) using a monochromated Al−Kα source. Survey and high-resolution spectra were obtained with pass energies of 100 and 20 eV. Further depth profiling was carried out through a repetitive process of Ar etching and an immediate XPS scan. The ultraporous ZnO films were deposited on SiO$_2$/Si substrates for SEM, XRD, and XPS analysis while on quartz substrates for UV−vis analysis.

The porosity, ε, was estimated from gravimetric and cross-sectional SEM analysis as previously suggested[56]

$$\varepsilon = 1 - \frac{T_{bulk}}{T_{SEM}} \tag{2}$$

where T_{SEM} is the thickness of the ZnO fractals measured from cross-sectional SEM, while T_{bulk} is the equivalent bulk thickness given by

$$T_{bulk} = 1 - \frac{V_{ZnO}}{A} = \frac{m}{\rho_{ZnO}A} \tag{3}$$

here, m is the mass of deposited material onto the substrate of the area A and ρ is the average density of the fractal media.

Sensing Measurements. The sensing measurements were performed as follows: VOCs (ethanol, 9.91 ppm in N$_2$ (BOC Ltd.); acetone, 10.1 ppm in N$_2$ (BOC Ltd.); ethylbenzene, 10 ppm in N$_2$ (BOC Ltd.); and propane, 10 ppm in N$_2$ (BOC Ltd.)) were controlled by mass flow controllers (Bronkhorst) and further diluted with simulated air (0.1 L min^{-1} O$_2$ + 0.4 L min^{-1} N$_2$ (BOC Ltd.)) to reach the desired concentration (from 2 ppb to 1 ppm), and the total gas flow rate was still kept at 0.5 L min^{-1}. The sensors were heated for 2 h at 300 °C in the continuous flow of synthetic air to desorb any atmospheric contamination before the start of each sensing experiment. The temperature of a stage in the sensing chamber (Linkam) was controlled by a temperature controller and the sample was illuminated through a quartz window by a solar simulator (NewSpec, LCS-100) with an AM1.5 filter glass. The dynamic response of the gas sensor was recorded by an electrochemical workstation (CHI 660E, USA) under a constant applied voltage of 1 V. Standard errors were calculated in the sensing measurements by performing sensing experiments at least 3 times with the same experimental conditions and the average responses are presented as the sensor response. The sensing response of the sensors was calculated as

$$\text{Sensor Response} = \left(\frac{I_{gas}}{I_{air}}\right) - 1 \tag{4}$$

where I_{gas} is the current in the presence of the target gas and I_{air} is the current in the air without the target gas. The target gas flowed into the sensing chamber for 15 min and was then switched off for 15 min. The response and recovery times were calculated using a threshold of 90% change in the response in the presence and absence of the target gas, respectively.

DFT Calculations. Spin-polarized DFT calculations were implemented using the Vienna ab initio simulation package (VASP)[57] with the core and valence electronic interactions being modeled using the projector augmented wave (PAW) method.[58] The Perdew−Burke−Ernzerhof (PBE) exchange-correlation function was employed.[59] The wave function was expanded with a kinetic energy cutoff of 500 eV and Gamma k-points were used. The Dudarev approach was implemented for the running of the DFT+U calculation, considering the electron self-interaction error in Ni and Zn. Hubbard's parameters of $U = 5.77$ for Ni in NiO,[60] $U = 10.0$, and $U = 7.0$ for Zn and O in ZnO were used.[61,62] Geometrical optimizations were achieved by relaxing all ionic positions and supercell vectors until the Hellman-Feynmann forces were less than 0.02 eV^{-1}. The dispersion correction was also considered in this study by using the DFT-D3 method.[53] The slab method was used to model NiO and ZnO surfaces with surface-bulk-like interactions, by fixing

the coordinates of the atoms in three bottom layers and relaxing the coordinates of the atoms in the three uppermost layers. The Gamma k-points of $3 \times 3 \times 1$ and $5 \times 3 \times 1$ were used for sampling the Brillouin zone for (2×2) NiO (002) and (2×2) ZnO $(10\bar{1}0)$ surfaces. A vacuum region of 20 was introduced in the direction of the z-axis to avoid interactions between the periodic images. The adsorption energies (E_{ads}) are computed using the following equation:

$$E_{ads} = E_{(slab+adsorbates)} - E_{slab} - E_{adsorbates} \tag{5}$$

■ ASSOCIATED CONTENT

Ⓢ Supporting Information

The Supporting Information is available free of charge at https://pubs.acs.org/doi/10.1021/acsami.3c12668.

Flame spray schematic, proposed reaction pathways and surface decomposition of ethanol on Ni$_x$O$_y$-ZnO nanoscale heterojunction networks, top-view and side-view SEM images, fractal analysis, XRD of pure NiO, NiO-ZnO, Tauc plots of pure ZnO, as-prepared and oxygen vacant NiO-ZnO, XPS survey and complete XPS depth profiles of Ni$_x$O$_y$-ZnO *p-n* nanoscale heterojunction networks; deconvoluted O 1s at various etching depths of as-prepared and oxygen vacant Ni$_x$O$_y$-ZnO; complete high resolution XPS spectra of O 1s, Zn 2p, and Ni 2p of as-prepared and oxygen vacant Ni$_x$;O$_y$-ZnO *p-n* nanoscale heterojunction networks, electronic band structure of Ni$_2$O$_3$, gas sensing mechanism for Ni$_x$O$_y$-ZnO *p-n* nanoscale heterojunctions, stability and humidity tests, XPS characteristic summary of O 1s at the top surface of as-prepared and oxygen vacant Ni$_x$O$_y$-ZnO *p-n* nanoscale heterojunctions, Fractions of oxygen species in O 1s of as-prepared and oxygen vacant Ni$_x$O$_y$-ZnO fractals at various etching depths (PDF)

■ AUTHOR INFORMATION

Corresponding Authors

Myung-Han Yoon − *School of Materials Science and Engineering, Gwangju Institute of Science and Technology (GIST), Gwangju 61005, Republic of Korea;* ⓘ orcid.org/0000-0001-7205-3054; Email: mhyoon@gist.ac.kr

Antonio Tricoli − *Nanotechnology Research Laboratory, Research School of Chemistry, College of Science, Australian National University, Canberra, Australian Capital Territory 2601, Australia; Nanotechnology Research Laboratory, Faculty of Engineering, University of Sydney, Sydney, New South Wales 2006, Australia;* ⓘ orcid.org/0000-0003-4964-2111; Email: antonio.tricoli@sydney.edu.au

Authors

Zain Ul Abideen − *Nanotechnology Research Laboratory, Research School of Chemistry, College of Science, Australian National University, Canberra, Australian Capital Territory 2601, Australia;* ⓘ orcid.org/0000-0002-2395-0178

Jun-Gyu Choi − *School of Materials Science and Engineering, Gwangju Institute of Science and Technology (GIST), Gwangju 61005, Republic of Korea*

Jodie A. Yuwono − *School of Chemical Engineering, The University of Adelaide, Adelaide, South Australia 5005, Australia*

Won-June Lee − *School of Materials Science and Engineering, Gwangju Institute of Science and Technology (GIST), Gwangju 61005, Republic of Korea;* ⓘ orcid.org/0000-0001-8756-0956

Krishnan Murugappan − *Nanotechnology Research Laboratory, Research School of Chemistry, College of Science, Australian National University, Canberra, Australian Capital Territory 2601, Australia; CSIRO, Mineral Resources, Clayton South, Victoria 3169, Australia;* ⊙ orcid.org/0000-0002-6845-4653

Priyank Vijaya Kumar − *School of Chemical Engineering, University of New South Wales, Sydney, New South Wales 2052, Australia;* ⊙ orcid.org/0000-0002-8203-7223

David R. Nisbet − *The Graeme Clark Institute and Department of Biomedical Engineering, The University of Melbourne, Melbourne, Victoria 3010, Australia;* ⊙ orcid.org/0000-0002-1343-0769

Thành Trần-Phú − *Nanotechnology Research Laboratory, Research School of Chemistry, College of Science, Australian National University, Canberra, Australian Capital Territory 2601, Australia;* ⊙ orcid.org/0000-0002-5935-3287

Complete contact information is available at:
https://pubs.acs.org/10.1021/acsami.3c12668

Author Contributions

[†]Z.U.A. and J.-G.C. contributed equally.

Notes

The authors declare no competing financial interest.

◼ REFERENCES

(1) Calow, J. T.; Deasley, P. J.; Owen, S. J. T.; Webb, P. W. A Review of Semiconductor Heterojunctions. *J. Mater. Sci.* **1967**, *2*, 88−96.

(2) Peng, J.; Kremer, F.; Walter, D.; Wu, Y.; Ji, Y.; Xiang, J.; Liu, W.; Duong, T.; Shen, H.; Lu, T.; Brink, F.; Zhong, D.; Li, L.; Lee Cheong Lem, O.; Liu, Y.; Weber, K. J.; White, T. P.; Catchpole, K. R. Centimetre-Scale Perovskite Solar Cells with Fill Factors of More Than 86 Per Cent. *Nature* **2022**, *601*, 573−578.

(3) Tu, Y.; Chen, S. Q.; Li, X.; Gorbaciova, J.; Gillin, W. P.; Krause, S.; Briscoe, J. Control of Oxygen Vacancies in ZnO Nanorods by Annealing and Their Influence on ZnO/PEDOT:PSS Diode Behaviour. *J. Mater. Chem. C. Mater.* **2018**, *6*, 1815−1821.

(4) Thomas, S. Gigahertz Heterojunction Bipolar Transistors on CMOS. *Nat. Electron.* **2022**, *5*, 826−826.

(5) Song, P.; Shen, J.; Ye, D.; Dong, B.; Wang, F.; Pei, H.; Wang, J.; Shi, J.; Wang, L.; Xue, W.; et al. Programming Bulk Enzyme Heterojunctions for Biosensor Development with Tetrahedral DNA Framework. *Nat. Commun.* **2020**, *11*, 838−848.

(6) Hou, H. L.; Anichini, C.; Samori, P.; Criado, A.; Prato, M. 2D Van der Waals Heterostructures for Chemical Sensing. *Adv. Funct. Mater.* **2022**, *32*, 2207065.

(7) Xue, X.; Russ, M.; Samkharadze, N.; Undseth, B.; Sammak, A.; Scappucci, G.; Vandersypen, L. M. K. Quantum Logic with Spin Qubits Crossing the Surface Code Threshold. *Nature* **2022**, *601*, 343−347.

(8) Li, X.; Zhang, Q.; Yu, J.; Xu, Y.; Zhang, R.; Wang, C.; Zhang, H.; Fabiano, S.; Liu, X.; Hou, J.; et al. Mapping the Energy Level Alignment at Donor/Acceptor Interfaces in Non-Fullerene Organic Solar Sells. *Nat. Commun.* **2022**, *13*, 2046−2055.

(9) Tsai, S. Y.; Hon, M. H.; Lu, Y. M. Fabrication of Transparent *p*-NiO/*n*-ZnO Heterojunction Devices for Ultraviolet Photodetectors. *Solid-State Electron.* **2011**, *63*, 37−41.

(10) Nasiri, N.; Bo, R.; Fu, L.; Tricoli, A. Three-Dimensional Nano-Heterojunction Networks: A Highly Performing Structure for Fast Visible-Blind UV Photodetectors. *Nanoscale* **2017**, *9*, 2059−2067.

(11) Chen, H.; Bo, R.; Shrestha, A.; Xin, B.; Nasiri, N.; Zhou, J.; Di Bernardo, I.; Dodd, A.; Saunders, M.; Lipton-Duffin, J.; et al. NiO−ZnO Nanoheterojunction Networks for Room-Temperature Volatile Organic Compounds Sensing. *Adv. Opt. Mater.* **2018**, *6*, 1800677.

(12) Wang, C.; Wang, T.; Wang, B.; Zhou, X.; Cheng, X.; Sun, P.; Zheng, J.; Lu, G. Design of α-Fe$_2$O$_3$ Nanorods Functionalized Tubular NiO Nanostructure for Discriminating Toluene Molecules. *Sci. Rep.* **2016**, *6*, 26432.

(13) Nakate, U. T.; Patil, P.; Na, S. I.; Yu, Y. T.; Suh, E. K.; Hahn, Y. B. Fabrication and Enhanced Carbon Monoxide Gas Sensing Performance of *p*-CuO/*n*-TiO$_2$ Heterojunction Device. *Colloids Surf. A. Physicochem. Eng. Asp.* **2021**, *612*, 125962−970.

(14) Li, J. N.; Zhao, F.; Zhang, L.; Zhang, M. Y.; Jiang, H. F.; Li, S.; Li, J. F. Electrospun Hollow ZnO/NiO Heterostructures with Enhanced Photocatalytic Activity. *RSC Adv.* **2015**, *5*, 67610−67616.

(15) Wang, Z. L.; Wang, L. Z. Role of Oxygen Vacancy in Metal Oxide based Photoelectrochemical Water Splitting. *Ecomat.* **2021**, *3*, e12075.

(16) Yang, Z.; Shi, Y.; Li, H.; Mao, C.; Wang, X.; Liu, X.; Liu, X.; Zhang, L. Oxygen and Chlorine Dual Vacancies enable Photocatalytic O$_2$ Dissociation into Monatomic Reactive Oxygen on BiOCl for Refractory Aromatic Pollutant Removal. *Environ. Sci. Technol.* **2022**, *56*, 3587−3595.

(17) Shi, Y.; Zhang, C.; Yang, Z.; Liu, X.; Zhang, X.; Ling, C.; Cheng, J.; Liang, C.; Mao, C.; Zhang, L. Interfacial Electrostatic Field Boosted Exciton Dissociation of Phosphorylated BiOBr for Efficient O$_2$ Activation and Chlorobenzene Degradation. *J. Phys. Chem. C* **2022**, *126*, 21847−21856.

(18) Wang, S.; Liao, W.; Su, H.; Pang, S.; Yang, C.; Fu, Y.; Zhang, Y. Review on the Application of Semiconductor Heterostructures in Photocatalytic Hydrogen Evolution: State-of-the-Art and Outlook. *Energy Fuels* **2023**, *37*, 1633−1656.

(19) Xu, Y. C.; Li, H. Z.; Sun, B. J.; Qiao, P. Z.; Ren, L. P.; Tian, G. H.; Jiang, B. J.; Pan, K.; Zhou, W. Surface Oxygen Vacancy Defect-Promoted Electron-Hole Separation for Porous Defective ZnO Hexagonal Plates and Enhanced Solar-Driven Photocatalytic Performance. *Chem. Eng. J.* **2020**, *379*, 122295−305.

(20) Shi, Y.; Shou, H.; Li, H.; Zhan, G.; Liu, X.; Yang, Z.; Mao, C.; Cheng, J.; Zhang, X.; Jiang, Y.; et al. Visible Light-Driven Conversion of Carbon-Sequestrated Seawater into Stoichiometric CO and HClO with Nitrogen-Doped BiOCl Atomic Layers. *Angew. Chem.* 2023, 62, e202302286.

(21) Zhang, T.; Wu, M. Y.; Yan, D. Y.; Mao, J.; Liu, H.; Hu, W. B.; Du, X. W.; Ling, T.; Qiao, S. Z. Engineering Oxygen Vacancy on NiO Nanorod Arrays for Alkaline Hydrogen Evolution. *Nano Energy* 2018, 43, 103−109.

(22) Li, G.; Zhang, H.; Meng, L.; Sun, Z.; Chen, Z.; Huang, X.; Qin, Y. Adjustment of Oxygen Vacancy States in ZnO and its Application in ppb-level NO_2 Gas Sensor. *Sci. Bull. (Beijing)* 2020, 65, 1650−1658.

(23) Abideen, Z. U.; Kim, J.-H.; Mirzaei, A.; Kim, H. W.; Kim, S. S. Sensing Behavior to ppm-level Gases and Synergistic Sensing Mechanism in Metal-Functionalized rGO-loaded ZnO Nanofibers. *Sensors Actuators B: Chem.* 2018, 255, 1884−1896.

(24) Zhang, J.; Li, J. The Oxygen Vacancy Defect of ZnO/NiO Nanomaterials Improves Photocatalytic Performance and Ammonia Sensing Performance. *Nanomaterials* 2022, 12, 433−453.

(25) Xu, J. J.; Li, S. J.; Li, L.; Chen, L. Y.; Zhu, Y. F. Facile Fabrication and Superior Gas Sensing Properties of Spongelike Co-doped ZnO Microspheres for Ethanol Sensors. *Ceram. Int.* 2018, 44, 16773−16780.

(26) Hamedani, N. F.; Mahjoub, A. R.; Khodadadi, A. A.; Mortazavi, Y. CeO_2 doped ZnO Flower-like Nanostructure Sensor Selective to Ethanol in Presence of CO and CH_4. *Sensors Actuators B: Chem.* 2012, 169, 67−73.

(27) Zhang, Y. Q.; Liu, Y. Y.; Zhou, L. S.; Liu, D. Y.; Liu, F. M.; Liu, F. M.; Liang, X. S.; Yan, X.; Gao, Y.; Lu, G. Y. The role of Ce Doping in Enhancing Sensing Performance of ZnO-based Gas Sensor by Adjusting the Proportion of Oxygen Species. *Sensors Actuators B: Chem.* 2018, 273, 991−998.

(28) Liu, J. Y.; Wang, T. S.; Wang, B. Q.; Sun, P.; Yang, Q. Y.; Liang, X. S.; Song, H. W.; Lu, G. Y. Highly Sensitive and Low Detection Limit of Ethanol Gas Sensor based on Hollow ZnO/SnO_2 Spheres Composite Material. *Sensors Actuators B: Chem.* 2017, 245, 551−559.

(29) Gholami, M.; Khodadadi, A. A.; Anaraki Firooz, A.; Mortazavi, Y. In_2O_3-ZnO Nanocomposites: High Sensor Response and Selectivity to Ethanol. *Sens. Actuat. B: Chem.* 2015, 212, 395−403.

(30) Illyaskutty, N.; Kohler, H.; Trautmann, T.; Schwotzer, M.; Pillai, V. P. M. Enhanced Ethanol Sensing Response from Nano-structured MoO_3:ZnO Thin Films and Their Mechanism of Sensing. *J. Mater. Chem. C. Mater.* 2013, 1, 3976−3984.

(31) Wang, L.; Ma, S. Y.; Xu, X. L.; Li, J. P.; Yang, T. T.; Cao, P. F.; Yun, P. D.; Wang, S. Y.; Han, T. Oxygen Vacancy-based Tb-doped SnO_2 Nanotubes as an Ultra-Sensitive Sensor for Ethanol Detection. *Sensors Actuators B: Chem.* 2021, 344, 130111−122.

(32) Wang, T.; Kou, X.; Zhao, L.; Sun, P.; Liu, C.; Wang, Y.; Shimanoe, K.; Yamazoe, N.; Lu, G. Flower-like ZnO Hollow Microspheres loaded with CdO Nanoparticles as High Performance Sensing Material for Gas Sensors. *Sensors Actuators B: Chem.* 2017, 250, 692−702.

(33) Liu, J.; Dai, M.; Wang, T.; Sun, P.; Liang, X.; Lu, G.; Shimanoe, K.; Yamazoe, N. Enhanced Gas Sensing Properties of SnO_2 Hollow Spheres Decorated with CeO_2 Nanoparticles Heterostructure Composite Materials. *ACS Appl. Mater. Interfaces* 2016, 8, 6669−77.

(34) Nasiri, N.; Bo, R. H.; Chen, H. J.; White, T. P.; Fu, L.; Tricoli, A. Structural Engineering of Nano-Grain Boundaries for Low-Voltage UV-Photodetectors with Gigantic Photo- to Dark-Current Ratios. *Adv. Opt. Mater.* 2016, 4, 1787−1795.

(35) Pargoletti, E.; Hossain, U. H.; Di Bernardo, I.; Chen, H.; Tran-Phu, T.; Lipton-Duffin, J.; Cappelletti, G.; Tricoli, A. Room-Temperature Photodetectors and VOC Sensors based on Graphene Oxide-ZnO Nano-Heterojunctions. *Nanoscale* 2019, 11, 22932−22945.

(36) Abideen, Z. U.; Choi, J. G.; Yuwono, J. A.; Kiy, A.; Kumar, P. V.; Murugappan, K.; Lee, W. J.; Kluth, P.; Nisbet, D. R.; Tran-Phu, T.; Yoon, M. H.; Tricoli, A. Oxygen Vacancies Engineering in Thick Semiconductor Films via Deep Ultraviolet Photoactivation for Selective and Sensitive Gas Sensing. *Adv. Electron. Mater.* 2023, 9, 2200905.

(37) Xu, Z. F.; Xu, K.; Lin, M. C. Ab Initio Kinetics for Decomposition/Isomerization Reactions of C_2H_5O Radicals. *Chem-PhysChem* 2009, 10, 972−82.

(38) Mavrikakis, M.; Barteau, M. A. Oxygenate Reaction Pathways on Transition Metal Surfaces. *J. Mol. Catal. A. Chem.* 1998, 131, 135−147.

(39) Chen, Y.; Gui, Y.; Chen, X. Adsorption and Gas-Sensing Properties of C_2H_4, CH_3, H_2, H_2O on Metal Oxides (CuO, NiO) modified SnS_2 Monolayer: A DFT Study. *Results Phys.* 2021, 28, 104680−691.

(40) Bartolomé, J.; Taeño, M.; Martínez-Casado, R.; Maestre, D.; Cremades, A. Ethanol Gas Sensing Mechanisms of *p*-type NiO at Room Temperature. *Appl. Surf. Sci.* 2022, 579, 152134−144.

(41) Yuan, Q. Z.; Zhao, Y. P.; Li, L. M.; Wang, T. H. Ab Initio Study of ZnO-Based Gas-Sensing Mechanisms: Surface Reconstruction and Charge Transfer. *J. Phys. Chem. C* 2009, 113, 6107−6113.

(42) Xu, G.; Zhang, L.; He, C.; Ma, D.; Lu, Z. Adsorption and Oxidation of NO on Various SnO_2 (1 1 0) Surfaces: A Density Functional Theory Study. *Sensors Actuators B: Chem.* 2015, 221, 717−722.

(43) Spencer, M. J. S. Gas Sensing Applications of 1D-Nano-structured Zinc Oxide: Insights from Density Functional Theory Calculations. *Prog. Mater. Sci.* 2012, 57, 437−486.

(44) Bo, R.; Zhang, F.; Bu, S.; Nasiri, N.; Di Bernardo, I.; Tran-Phu, T.; Shrestha, A.; Chen, H.; Taheri, M.; Qi, S.; Zhang, Y.; Mulmudi, H. K.; Lipton-Duffin, J.; Gaspera, E. D.; Tricoli, A. One-Step Synthesis of Porous Transparent Conductive Oxides by Hierarchical Self-Assembly of Aluminum-Doped ZnO Nanoparticles. *ACS Appl. Mater. Interfaces* 2020, 12, 9589−9599.

(45) Fusco, Z.; Tran-Phu, T.; Cembran, A.; Kiy, A.; Kluth, P.; Nisbet, D.; Tricoli, A. Engineering Fractal Photonic Metamaterials by Stochastic Self-Assembly of Nanoparticles. *Adv. Photonics Res.* 2021, 2, 2100020.

(46) Tran-Phu, T.; Daiyan, R.; Leverett, J.; Fusco, Z.; Tadich, A.; Di Bernardo, I.; Kiy, A.; Truong, T. N.; Zhang, Q.; Chen, H.; Kluth, P.; Amal, R.; Tricoli, A. Understanding the Activity and Stability of Flame-Made Co_3O_4 Spinels: A Route Towards the Scalable Production of Highly Performing OER Electrocatalysts. *Chem. Eng. J.* 2022, 429, 132180−192.

(47) Monshi, A.; Foroughi, M. R.; Monshi, M. R. Modified Scherrer Equation to Estimate More Accurately Nano-Crystallite Size Using XRD. *W. J. Nano Sci. Eng.* 2012, 02, 154−160.

(48) Wagner, C. D.; Gale, L. H.; Raymond, R. H. Two-Dimensional Chemical State Plots: A Standardized Data Set for Use in Identifying Chemical States by X-ray Photoelectron Spectroscopy. *Anal. Chem.* 1979, 51, 466−482.

(49) Xie, X. J.; Si, R. J.; Zheng, J.; Wei, K.; Zheng, X. Y.; Chen, C.; Wang, C. C. Synthesis of ZnO/NiO Hollow Spheres and Their Humidity Sensing Performance. *J. Alloys Compd.* 2021, 879, 160487−494.

(50) Nasiri, N.; Bo, R.; Wang, F.; Fu, L.; Tricoli, A. Ultraporous Electron-Depleted ZnO Nanoparticle Networks for Highly Sensitive Portable Visible-Blind UV Photodetectors. *Adv. Mater.* 2015, 27, 4336−43.

(51) Tricoli, A.; Pratsinis, S. E. Dispersed Nanoelectrode Devices. *Nat. Nanotechnol.* 2010, 5, 54−60.

(52) Abokifa, A. A.; Haddad, K.; Fortner, J.; Lo, C. S.; Biswas, P. Sensing Mechanism of Ethanol and Acetone at Room Temperature by SnO_2 Nano-Columns Synthesized by Aerosol Routes: Theoretical Calculations Compared to Experimental Results. *J. Mater. Chem. A. Mater.* 2018, 6, 2053−2066.

(53) Grimme, S.; Antony, J.; Ehrlich, S.; Krieg, H. A Consistent and Accurate Ab Initio Parametrization of Density Functional Dispersion Correction (DFT-D) for the 94 Elements H-Pu. *J. Chem. Phys.* 2010, 132, 154104.

(54) Fusco, Z.; Rahmani, M.; Bo, R.; Verre, R.; Motta, N.; Kall, M.; Neshev, D.; Tricoli, A. Nanostructured Dielectric Fractals on Resonant Plasmonic Metasurfaces for Selective and Sensitive Optical Sensing of Volatile Compounds. *Adv. Mater.* **2018**, *30*, 1800931.

(55) Stadelmann, P. A. Ems - a Software Package for Electron-Diffraction Analysis and Hrem Image Simulation in Materials Science. *Ultramicroscopy* **1987**, *21*, 131−145.

(56) Fusco, Z.; Rahmani, M.; Tran-Phu, T.; Ricci, C.; Kiy, A.; Kluth, P.; Della Gaspera, E.; Motta, N.; Neshev, D.; Tricoli, A. Photonic Fractal Metamaterials: A Metal-Semiconductor Platform with Enhanced Volatile-Compound Sensing Performance. *Adv. Mater.* **2020**, *32*, 2002471.

(57) Kresse, G.; Furthmuller, J. Efficiency of Ab-Initio Total Energy Calculations for Metals and Semiconductors Using a Plane-Wave Basis Set. *Comput. Mater. Sci.* **1996**, *6*, 15−50.

(58) Blochl, P. E. Projector Augmented-Wave Method. *Phys. Rev. B: Condens. Matter* **1994**, *50*, 17953−17979.

(59) Perdew, J. P.; Burke, K.; Ernzerhof, M. Generalized Gradient Approximation Made Simple. *Phys. Rev. Lett.* **1996**, *77*, 3865−3868.

(60) Cococcioni, M.; de Gironcoli, S. Linear Response Approach to the Calculation of the Effective Interaction Parameters in the LDA+U Method. *Phys. Rev. B: Condens. Matter* **2005**, *71*, 035105−121.

(61) Lee, Y.-S.; Peng, Y.-C.; Lu, J.-H.; Zhu, Y.-R.; Wu, H.-C. Electronic and Optical Properties of Ga-doped ZnO. *Thin Solid Films* **2014**, *570*, 464−470.

(62) Deng, X.-Y.; Liu, G.-H.; Jing, X.-P.; Tian, G.-S. On-Site Correlation of *p*-electron in d^{10} Semiconductor Zinc Oxide. *Int. J. Quantum Chem.* **2014**, *114*, 468−472.